ARMA 17-517

Modeling Dynamic Shear Rupture and Microseismic Source Responses on Discontinuities Induced by Quasi-Static Flow-Driven Stress in Fractured Porous Media

Jin, L. and Zoback M.D.
Department of Geophysics, Stanford University, CA, U.S.A.
Pourpak, H. and Onaisi, A.
CSTJF, Total S.A., Pau Cedex, France

ABSTRACT: The problem of dynamic shear (mode II) rupture on a non-growing fracture embedded in a solid continuum is traditionally solved using a standard split-node finite element method by permitting displacement discontinuity on the fracture while imposing contact constraint via a Lagrangian multiplier or a penalty regularization. In the presence of fluid pressure, this framework can be adjusted accordingly using an effective stress formulation, hence, in principle, can be used for modeling a rupture process in a fluid-filled porous medium and the associated microseismic source responses. However, if the porous medium is subjected to pressure spatial variations, the pressure gradient then acts as a body force, as naturally predicted by the force balance law, generating additional flow-driven stress in the medium. Moreover, when fractures are present, the pressure gradient across fractures is often discontinuous, further complicating the flow-driven stress state. Such coupling effects are rarely included in currently available rupture codes, hence limiting their applications to fluid-induced seismicity. In this study, we take into account flow-driven stress and provide a numerical modeling framework for fluid-induced quasi-static triggering and dynamic shear rupture processes on pre-existing discontinuities. Through a simple configuration in which two natural fractures intersect a hydraulic fracture, we illustrate how a flow-driven rupture process can be used to understand microseismic source responses, estimate permeability enhancement, as well as provide potential explanations for some curious injection-related geophysical observations.

Keywords: Fluid Flow; Poroelasticity; Dynamic Shear Rupture; Induced Seismicity; Microseismicity; Fractured Porous Media; Finite Element Method

1. INTRODUCTION

Fluid injection and withdrawal can induce seismicity on a wide range of scales (Ellsworth, 2013). Occurrence of such seismic events poses major environmental and public concerns in activities including CO2 capture and sequestration, wastewater injection and conventional hydrocarbon production. On the other hand, events at a much smaller scale, known as microseismic events, are considered as an important mechanism to enhance fluid flow and are stimulated in unconventional hydrocarbon reservoirs and geothermal systems with ultra-low permeability. In any case, an understanding of the associated physical process is crucial for effective control and management of these fluid-induced (micro)seismic events.

Triggering of seismicity (shear failure) on a pre-existing fracture embedded in a fluid-filled porous medium is traditionally attributed to a de-coupled hydro-mechanical process, in which the effective normal stress on the fracture simply decreases by the amount of fluid overpressure, whereas the shear stress remains unchanged. This results in a direct increase in the Coulomb stress, which, when driven to positive, signify the onset of fracture slip. However, seismicity has been widely observed outside the region subjected to a direct pore pressure perturbation (e.g., Stark & Davis, 1996; Megies & Wassermann, 2014). These events are remotely triggered and are also referred to as 'dry events' in the microseismic literature. Even within the pressure-perturbed region, the stress history of a known fracture sometimes deviates from an anticipated path. For example, decrease of pore pressure in a reservoir can induce faulting as opposed to prohibit it (Zoback & Zinke, 2002). These observations cannot be adequately explained by the de-coupled approach, motivating a consideration of hydro-mechanical coupling (also referred to as pore pressure-stress coupling (Hillis, 2000)) for induced seismicity problems, mostly within the framework of linear poroelasticity (e.g., Wang,

2000). This theory predicts a full coupling between the mean stress (or volumetric strain) and the pore pressure gradient. In terms of fluid-to-solid coupling, it predicts that the pressure gradient acts as an equivalent body force and dictates a flow-driven full stress tensor within the medium. Some classical analytical solutions of flow-driven stress have been derived for simple configurations in which an isotropic, homogenous and linearly elastic porous medium is subjected to pressure from a point source (Cleary, 1977; Rudnicki, 1986; Altmann et al., 2014), a line source (Marck et al., 2015), or a layered source (Segall, 1985; Segall, 1998). These analytical solutions are indeed very useful as paradigms for explaining, for example, remotely triggered events from a coupled point of view. However, they are intrinsically unable to reveal flow and flow-stress coupling on discontinuities, hence have limited applications to induced seismicity in fractured porous media, especially in cases like stimulation of unconventional reservoirs where microseismicity can occur directly on fractures undergoing changes in pressure and flow-driven stress.

This motivates some recent numerical modeling studies of fluid-induced seismicity in a coupled manner to investigate the role of flow-driven stress under more realistic settings, typically involving pre-existing faults at a reservoir scale or a basin scale (e.g., Murphy et al., 2013; Chang & Segall, 2016; Fan et al., 2016; Deng et al., 2016). In the case of modeling fluid-induced microseismicity, a common approach is to model changes in fluid pressure and stress, and the element-wise effective stress state is extracted and compared against a failure criterion for determining the occurrence of a microseismic event (e.g., Baisch et al., 2010; Wassing et al., 2014). Such modeling can provide a synthetic microseismic catalog containing source time, location, stress drop and moment magnitude, which offers some insights into event spatial-temporal and statistical characteristics and their relation to model inputs (Goertz-Allmann & Wiemer, 2012). The synthetic catalog can also be compared against laboratory or field observations for calibration of model physics, including, e.g., appropriate medium rheology (Heinze et al., 2015), effect of stress transferring (Catalli et al., 2016; Rinaldi & Nespoli, 2016), and effect of poroelastic coupling (Riffault et al., 2016). However, all these studies exclusively focus on inter-seismic quasi-static triggering processes, and are not concerned with co-seismic dynamic rupture processes (dynamic as inertial in our paper). Note also that in all these models, regardless of the scale of induced seismicity, faults and fractures are represented as either stochastic properties or equi-dimensional entities permitted to follow different rheologies, rather than being resolved as true discontinuities, thus these models are fundamentally unable to reveal seismic source mechanisms.

In this study, we model fluid-induced (micro)seismicity on pre-existing discontinuities embedded in a fluid-filled poroelastic medium. Our modeling accounts for three primary processes, including fluid flow, flow-driven quasi-static triggering and flow-driven co-seismic dynamic shear rupture. We do not attempt to solve the fully coupled quasi-static poroelastic equation (for the triggering problem), nor the fully coupled poro-elastodynamic equation (for the rupture problem), both of which can suffer from stability issues rising from certain interpolation schemes (e.g., White & Borja, 2008) and constraints on discontinuities (Béchet et al., 2009). Instead, we focus on explicit representation of known *a priori* discontinuities and seek for numerical solutions in a fluid-to-solid coupled manner, in which the fluid pressure gradient drives changes in deformation and slip, but these changes are not fed back into changes of fluid pressure. In addition, we do not include any non-linearity arising from permeability changes, plasticity and rate-and-state frictional behavior on discontinuities. Lastly, we exclude any nucleation effect and fracture growth from the rupture process. Upon such stipulations, we shall then utilize the modeling to investigate microseismic source responses and permeability changes on the discontinuities, and probe their sensitivity to the hydraulic properties of these discontinuities.

2. PROBLEM STATEMENT

2.1. Model Domain

We consider a 2D arbitrary domain $\Omega \subset \mathbb{R}^2$ composed of a porous matrix domain $\Omega_m \subset \mathbb{R}^2$ and a discrete fracture network (DFN) $\Omega_f = \bigcup_{i=1}^{n_f} \Omega_{f_i}$, $\Omega_{f_i} \subset \mathbb{R}^2$, such that $\Omega = \Omega_m \cup \Omega_f$. Here, n_f is the number of fracture. Because fracture thickness is usually orders of magnitude lower than typical mesh size of the matrix, for computational purpose, we do not resolve details within the thickness of a fracture. Instead, we represent a fracture as a reduced-dimensional internal discontinuity, $\Omega_{f_i} \to \partial f_i \subset \mathbb{R}^1$. Fracture thickness will be implicitly accounted for throughout computation. Let Ω be externally bounded by $\partial\Omega$. The Dirichlet and Neumann boundaries are denoted as $\partial\Omega_p$ and $\partial\Omega_v$ for the flow problem, and as $\partial\Omega_u$ and $\partial\Omega_t$ for the solid problem, respectively. $\partial\Omega_p \cap \partial\Omega_v = \emptyset$, $\partial\Omega_p \cup \partial\Omega_v = \partial\Omega$; $\partial\Omega_u \cap \partial\Omega_t = \emptyset$, $\partial\Omega_u \cup \partial\Omega_t = \partial\Omega$; $\partial\Omega_p \neq \emptyset$, $\partial\Omega_u \neq \emptyset$. We also neglect intersections among individual fractures and between a fracture and the external boundary.

2.2. Conservation and Constitutive Laws

We are interested in the following three problems: a weakly discontinuous transient fluid flow problem describing pressure diffusion but not mean stress diffusion, a continuous solid problem describing flow-driven quasi-static triggering, and a strongly

discontinuous solid problem describing flow-driven co-seismic dynamic shear rupture and seismic source responses. Correspondingly, we solve three governing equations over Ω, including the conservation of mass in the fully saturated discrete fracture-porous matrix system, the quasi-static force balance law for the fluid-solid mixture prior to shear failure, and the conservation of linear momentum for the mixture since the onset of dynamic shear rupture. In the fluid problem, the fluid is assumed to be incompressible; Ω is dictated by a Darcy flow regime within Ω_m and by a lower-dimensional Poiseuille flow regime along $\partial f_i (i=1\sim n_f)$; the mass exchange between Ω_m and Ω_f is accounted for by either admitting flow weak discontinuities (discontinuity in flow velocity) across highly conductive fractures, or enforcing the local mass conservation as interface conditions on fractures isolated from external fluid sources. In the two solid problems, no separate rheologies are introduced for Ω_m and Ω_f; instead, a single linearly elastic constitutive law is assumed over Ω. The fluid-to-solid coupling is achieved by passing the pressure gradient as an equivalent body force to both solid problems at all time steps. Details are given in Jin & Zoback (2016; 2017, in review).

2.3. Failure Criterion and Contact Condition

We adopt the linear Mohr-Coulomb shear failure criterion for determining the onset time of dynamic shear rupture, t^*. Shear rupture occurs when the Coulomb stress, defined as below using the fracture normal stress and the maximum shear stress, is driven from negative to 0:

$$CS_{f_i} = \left[\left\| \boldsymbol{\sigma}'(t_{f_i}^*) \cdot \underline{n}_{f_i} \right\|^2 - \left(\boldsymbol{\sigma}'(t_{f_i}^*) : \underline{n}_{f_i} \otimes \underline{n}_{f_i} \right)^2 \right]^{\frac{1}{2}} - \mu_{f_i} \left(\boldsymbol{\sigma}'(t_{f_i}^*) : \underline{n}_{f_i} \otimes \underline{n}_{f_i} \right) - c_{f_i} = 0 \quad (1)$$

where, $\boldsymbol{\sigma}'$ is the effective stress tensor, $\underline{n}$ indicates the unit fracture normal vector, c_f is the cohesion, and μ_f is the frictional coefficient, and is assumed to be constant in this study. Subscript f_i denotes a quantify associated with the i^{th} fracture.

The overall stress on the fracture of length l is calculated as:

$$\boldsymbol{\sigma}(t_{f_i}^*) = \frac{1}{l_i} \int_{\Omega_{f_i}} \boldsymbol{\sigma}'(\underline{x}, t_{f_i}^*) d\tau, \quad \underline{x} \in \partial f_i \quad (2)$$

where $d\tau$ is the incremental length along the i^{th} fracture.

Upon onset of shear rupture on a fracture, we impose the contact constraint as following, written in an integral form:

$$\int_{\partial f_i} \varphi [\![\underline{u}(\underline{x}, t)]\!] \cdot \underline{n}_{f_i} = 0 \qquad t \geq t_{f_i}^* \quad (3)$$

where φ is an arbitrary constant, and $u(\underline{x}, t)$ is the displacement. $[\![\cdot]\!] := (\cdot)|_{\Gamma^+} - (\cdot)|_{\Gamma^-}$ denotes a jump in a quantity across a discontinuity.

2.4. Boundary and Initial Conditions

Standard Dirichlet and Neumann boundary conditions are prescribed on the external boundary for the flow problem as:

$$\begin{aligned} p(\underline{x}) &= p_g \qquad \forall \underline{x} \in \partial\Omega_p \\ -\underline{n} \cdot \underline{v}(\underline{x}) &= v_h \quad \forall \underline{x} \in \partial\Omega_v \end{aligned} \quad (4)$$

And for the quasi-static triggering problem as:

$$\begin{aligned} \underline{u}(\underline{x}) &= \underline{u}_g \qquad \forall \underline{x} \in \partial\Omega_u \\ \underline{n} \cdot \boldsymbol{\sigma}(\underline{x}) &= \underline{t}_h(x) \quad \forall \underline{x} \in \partial\Omega_t \end{aligned} \quad (5)$$

For the dynamic shear rupture problem, one can choose among different non-reflecting boundary conditions (Givoli, 1991) for minimizing spurious reflections on $\partial\Omega$. For example, the classical Lysmer absorbing boundary condition (Lysmer & Kuhlemeyer, 1969) can be implemented by adding a diagonal damping matrix in the final semi-discrete form of the equation. However, in this study, it is not our focus to deal with spurious reflections on $\partial\Omega$. Instead, we circumvent the problem of by turning off the simulation before any dynamic change reaches the boundary, and use Eq.(5) as the boundary condition.

In the flow problem, because we are interested in solving for excess pressure, the initial condition simply reads:

$$p(\underline{x}, 0) = 0 \ \forall \underline{x} \in \Omega \setminus \partial\Omega_p \quad (6)$$

For the dynamics rupture problem, the initial condition reads:

$$\begin{aligned} \underline{u}^{DY}(\underline{x}, t^*) &= \underline{u}^{QS}(\underline{x}, t^*) \qquad \forall \underline{x} \in \Omega \setminus \partial\Omega_u \\ \dot{\underline{u}}^{DY}(\underline{x}, t^*) &= \underline{0} \qquad \forall \underline{x} \in \Omega \setminus \partial\Omega_u \end{aligned} \quad (7)$$

Here, superscripts *DY* and *QS* indicate dynamic and quasi-static, respectively. Note, the result from the rupture modeling will include a part from the previous quasi-static triggering phase. One can of course subtract it from the result to get the part due to solely the dynamic rupture phase.

2.5. Discretization, Interpolation and Time Integration

The described problems are solved using a customized code newly developed by Jin & Zoback (2016; 2017, in review). Here, we do not attempt to present the full details. The fluid problem is discretized using a so-called hybrid-dimensional finite element method, based on an assumption of transversal uniformity in flow velocity

within fractures. A mixed-dimensional low-order interpolation of the fluid pressure is employed and has been shown to be reconcilable through the use of linear elements and appropriate compensation procedures. For a 1D fracture line element tangentially conforming to a 2D matrix element (they constitute a hybrid element), the fracture nodes bear no additional degrees of freedom, but share values with a subset of the matrix nodes of this hybrid element. The continuous and discontinuous solid problems are discretized using a standard finite element method (e.g, Hughes, 2012) and a split-node finite element method (e.g., Borja, 2013), respectively. A low-order interpolation of the displacement is adopted in both problems. In the latter, the contact condition Eq.(3) is enforced via a Lagrangian multiplier, which is interpolated using reduced-dimensional low-order elements.

In addition, to suppress spurious oscillations of high frequencies on rupture sources, we add the classical mass- and stiffness- proportionate viscous damping matrix, known as the Rayleigh damper (see e.g., Liu & Gorman, 1995) into the rupture problem. It reads:

$$\mathbf{C} = a\mathbf{M} + b\mathbf{K} \tag{8}$$

where a and b are the Rayleigh Damping Coefficients, $\mathbf{M}$ and $\mathbf{K}$ are the mass matrix and the stiffness matrix, respectively.

Since at each time step we need to pass the interpolated pressure gradient as an equivalent body force to both solid problems, we highlight here the term (after weak formulation) that is responsible for generating flow-driven stress. For a linear triangular element, it takes the following element-wise expression:

$$\iint_{\Omega_m^e} \mathbf{N}^{eT} \alpha \nabla \underline{N}^e \hat{\zeta}^e d\Omega = \frac{1}{3}\alpha A^e \left[f_{px} \;\; f_{py} \;\; f_{px} \;\; f_{py} \;\; f_{px} \;\; f_{py} \right]^T$$
$$f_{px} = \left(N^e_{1,x}\zeta^e_1 + N^e_{2,x}\zeta^e_2 + N^e_{3,x}\zeta^e_3 \right)$$
$$f_{py} = \left(N^e_{1,y}\zeta^e_1 + N^e_{2,y}\zeta^e_2 + N^e_{3,y}\zeta^e_3 \right) \tag{9}$$

where, $\mathbf{N}^e$ and $\underline{N}^e$ are the elemental shape functions in the solid problems and in the fluid problem, respectively, $\hat{\zeta}^e = [\zeta^e_1, \zeta^e_2, \zeta^e_3]$ is the element-wise nodal fluid pressure, A^e is the area of the element, and α is the Biot coefficient, and subscript T stands for transpose.

Finally, we use finite difference discretization schemes for advancing the solutions in time. For the transient fluid flow problem, we choose the fully implicit backward Euler scheme, which offers unconditional stability and first-order accuracy. For the co-seismic dynamic rupture problem, we opt for the implicit and unconditionally stable scheme from the well-known Newmark family method. This scheme offers a second-order accuracy. To show the difference, we denote the time increment as dt and δt, respectively, for the two problems. Note dt and δt can vary by orders of magnitude, $dt \gg \delta t$.

3. NUMERICAL EXAMPLES

3.1. *Model Domain and Nominal Parameters*

We create a 200m×200m model domain, see Fig.1. One horizontal hydraulic fracture of length 40m intersects two natural fractures of length $40\sqrt{2}$ and dipping at 45°. All three fractures are pre-defined. The Dirichlet and Neumann boundaries for both the flow problem and the solid problems, as is shown in 2.4, are labeled. In this study, injection is modeled as the Dirichlet boundary condition by prescribing a constant fluid pressure at the injection point located at the center of the hydraulic fracture. For observing the seismic waveforms, we distribute two sets of seismometers within the domain in a manner such that both sets allow a good sampling of a full focal sphere. Using the Delaunay triangulation, the domain is discretized into 12800 triangular elements conforming to all three fractures.

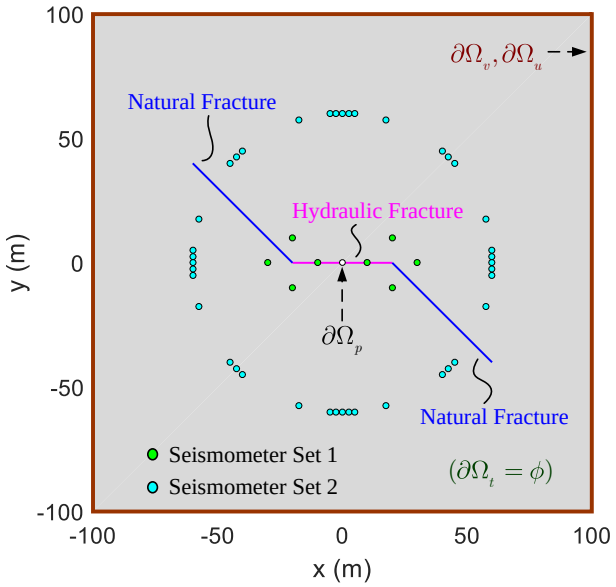

Fig. 1. A 2D model domain with two natural fractures intersected by a hydraulic fracture

In this study, because we assume linear flow regimes and linear elasticity within the domain, we will restrict our focus only on excess fluid pressure (changes in fluid pressure relative to an arbitrary initial pore pressure field) in the fluid problem, and subsequently changes due to flow-driven stress in the two solid problems. A complete list of model nominal parameters is given in table 1. To investigate the sensitivity of microseismic source response to fracture hydraulic properties, we devise four different cases in which the aperture of the two natural fractures spans over four orders of

magnitude, while all other parameters are held the same. Defining diffusivity along a certain direction as $k/(\eta C\phi)$, we then obtain the tangential diffusivity of the natural fractures as 6.67×10^{2}, 6.67, 6.67×10^{-2} and 6.67×10^{-4} m^2/s in the four cases where the tangential permeability is calculated via the cubic law. In all cases, the matrix diffusivity is 1.3×10^{-3} m^2/s on average along both X and Y directions, and the diffusivity of the hydraulic fracture is 6.67×10^{2} m^2/s.

Table 1. Model nominal parameters

Parameter		Value
ϕ_{m0}	Matrix initial porosity	0.24~0.26, random
C_{fi}(i=1~3)	Fracture compressibility	10^{-8} Pa^{-1}
C_m	Matrix compressibility	10^{-9} Pa^{-1}
$\mathbf{k}_m$	Matrix permeability	[1 0; 0 1] $\times10^{-3}$ D
b_i(i=1, HF)	Fracture aperture	1.1×10^{-3}m
b_i (i=2~3, NF)	Fracture aperture	Case 1: 1.1×10^{-4}m Case 2: 1.1×10^{-5}m Case 3: 1.1×10^{-6}m Case 4: 1.1×10^{-7}m
η	Fluid viscosity	10^{-3} Pa·s
p_g	Flow Dirichlet boundary value	5 MPa (above initial pressure)
v_h	Flow Neumann boundary value	0
s	External fluid source	0
dt	Time increment (flow)	Case 1~2: 30 sec Case 3~4: 500 sec
α	Biot coefficient	0.8
$\underline{u_g}$	Solid Dirichlet boundary value	$\underline{0}$
$\underline{f_b}$	Body force	$\underline{0}$
λ	Lame's constant of the mixture	16 GPa
μ	Shear modulus of the mixture	16 GPa
μ_{fi}(i=2~3)	Fracture frictional coefficient	0.6
c_{fi}(i=2~3)	Fracture cohesion	0
ρ_{mix}	Density of the mixture	2500 kg/m^3
a	Rayleigh damping coefficients	0.001
b		2.0×10^{-5}
δt	Time increment (rupture)	0.0002 sec

3.2. *Fluid Flow*

In the four cases, we simulate flow injection for 4.5, 14.5, and 1500 minutes. Fig.1 shows a time slice of the spatial distribution of the excess fluid pressure, colored in linear scale, at the end of simulation for each case. A close-up view on the area near the hydraulic fracture-natural fracture intersection is also shown. The result of Case 4 is nearly identical to that of Case 3, hence it is not shown here. In Case 1, the pressure spread into all the fractures and reaches injection pressure almost instantaneously. In Case 2, the natural fractures act as preferred flow paths after the pressure increases first in the hydraulic fracture. In Case 3 and 4, however, the fluid pressure diffuses away primarily from the hydraulic fractures into the matrix, and the natural fractures barely alter the flow path.

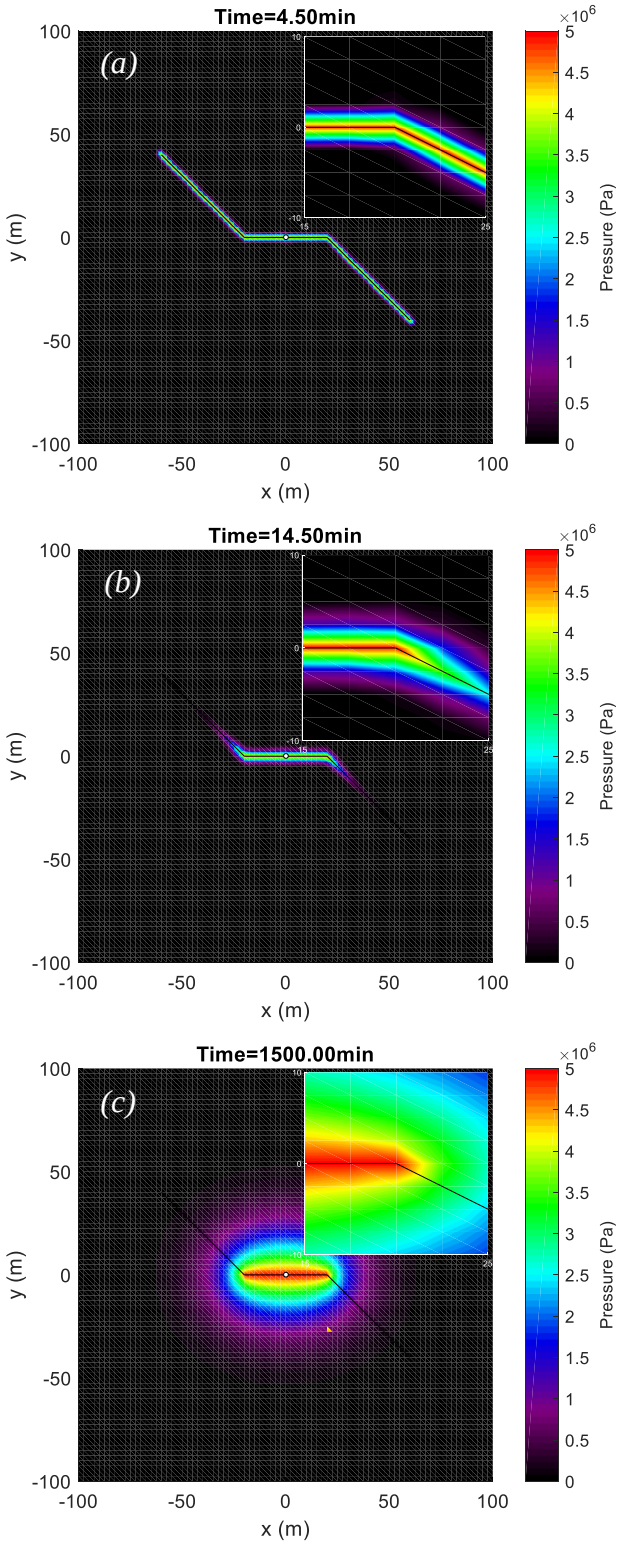

Fig.2. Spatial distribution of the excess fluid pressure at the end of simulation in each case. The time is shown at the top. (a) Case 1; (b) Case 2; (c) Case 3 (Case 4 identical).

3.3. Flow-Driven Quasi-Static Triggering

In each case, the flow-driven deformation and the full stress tensor are calculated at each time step as is employed in the flow modeling, and is superimposed onto an arbitrary initial stress tensor, which is assumed to be [6 0; 0 2] MPa herein for this study. We then compute the effective normal stress and shear stress resolved on the two natural fractures (stress state identical on the two natural fractures due to the symmetry of the problem), and track the evolution of the stress state in relation to the failure line. As an example, Fig.3 gives the evolution of the stress state on the two natural fractures in Case 2, colored by the time since fluid injection. If using a hydro-mechanical de-coupled approach, one would expect a perfectly leftward stress path, with the amount of movement between two consecutive time steps simply equal to the incremental fluid pressure. However, as is shown here by the complex stress path, this is not the case if we consider the stress to be driven by the pressure gradient. From Eq.(1), we are able to determine the onset of shear rupture to be at 11.0 minutes. The flow-driven displacement field and stress fields at the time of activation t^* in Case 2 are shown in Fig.4. The displacement will be used as the initial condition for the dynamic rupture modeling. The stress fields show a tensile stress state near the fractures, but a compressive stress state in the rest of the domain, along both X and Y directions. In addition, shear stress is also present.

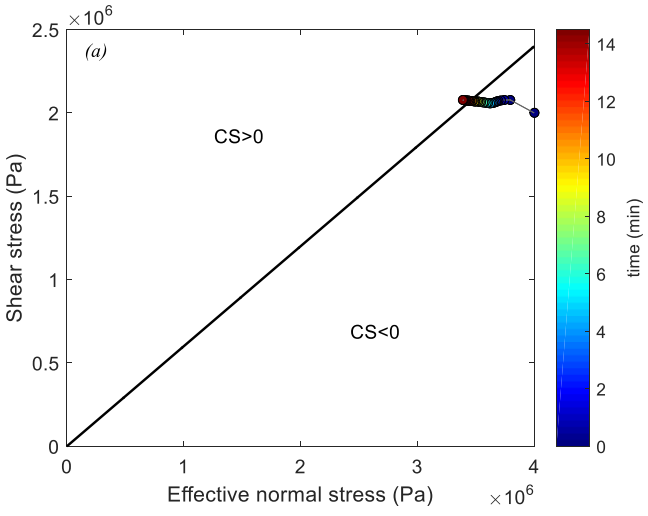

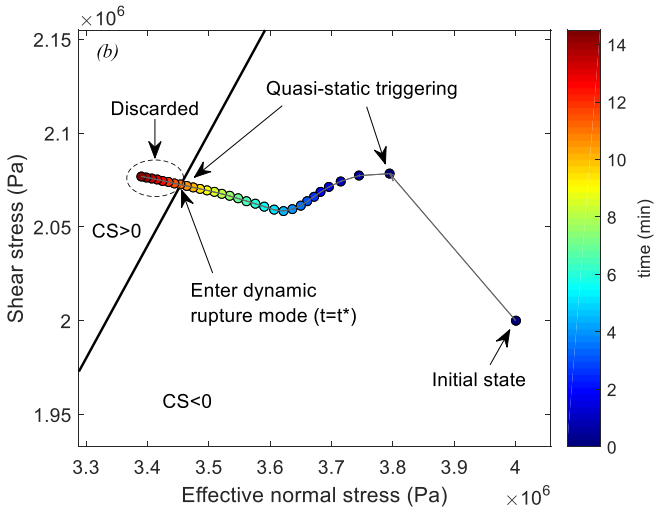

Fig.3. Evolution of stress state on the two natural fractures in relation to the shear failure since injection in Case 2. The fractures undergo a complex quasi-static stress history before being activated. (a)An overall view; (b) A close-up view.

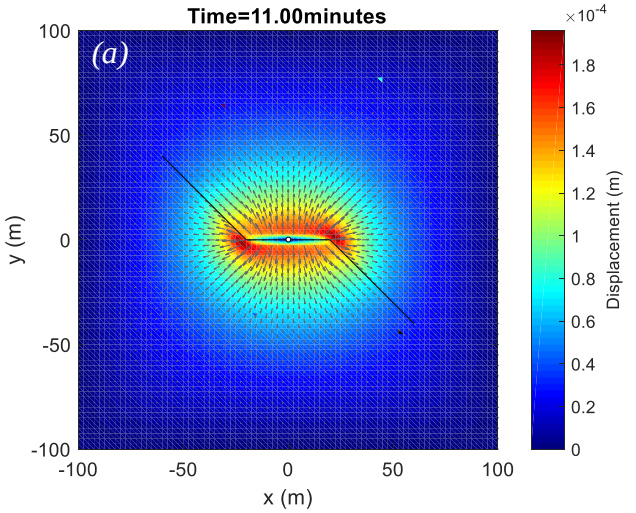

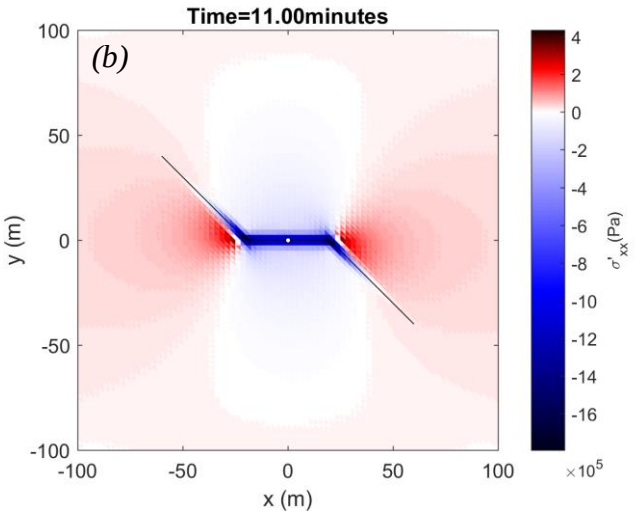

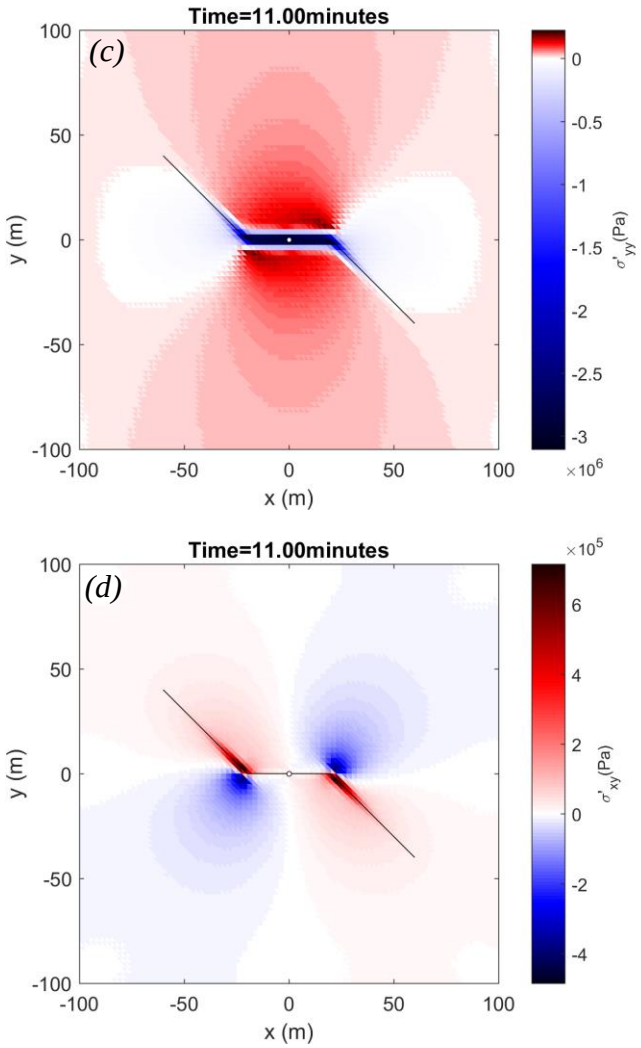

Fig.4. Flow-driven mechanical changes relative to an arbitrary initial state at the time of activation in Case 2. (a) Displacement, color indicates the magnitude and vectors indicate directions. This displacement field is used as the initial conditions for dynamic rupture modeling; (b)&(c) Effective normal stress along X and Y; (d) Shear stress.

3.4. Flow-Driven Co-Seismic Dynamic Shear Rupture

After entering the dynamic mode, we simulate the shear rupture process for 0.01 second for all cases. As an example, Fig.5 depicts the dynamic wave field for Case 1 and Case 2. Only the particle velocity along X is shown for illustration. The four selected time steps are chosen to be 0.001, 0.003, 0.007 and 0.01 second after the onset of rupture. Note we do not take account the rupture nucleation effect. Once the rupture occurs on a fracture, nodes are split along the full length of the fracture. However, because of the different fluid pressure distribution shown in Fig.2, the rupture behavior still differs significantly between these two cases. In Case 1, instantaneous pressurization and the resulting relatively uniform flow-driven stress state along the natural fractures lead to an immediate rupture initiation along the full length of the fractures, and the maximum particle velocity occurs at both fracture tips. In Case 2, the maximum particle velocity is observed where the maximum fluid pressure is, and the waves are predominantly sourced from that location.

We also derive the temporal evolution of slip velocity along a fracture by calculating the relative particle velocity on the two faces of the fracture. As an example, the result for Case 2 is shown in Fig.6. Distribution of slip velocity (magnitude) along the two natural fractures are shown at 10 different time steps since the inception of dynamic rupture. As the time progresses, peak slip velocity travels along the fracture from one tip (where the maximum fluid pressure is) to the other while decaying in magnitude. Figure 7 gives the slip velocity evolution in time (using result at all time step) at all pairs of nodal points on the natural fractures. The slip velocity is on the order of 0.01~0.1 m/s, peaking at nearly 0.8m/s.

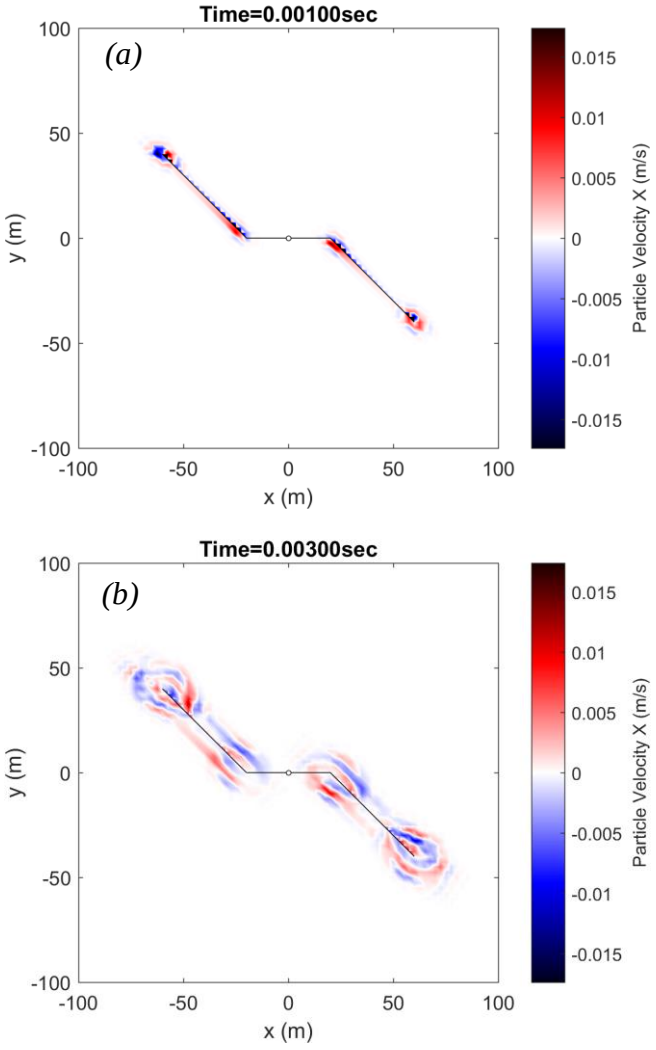

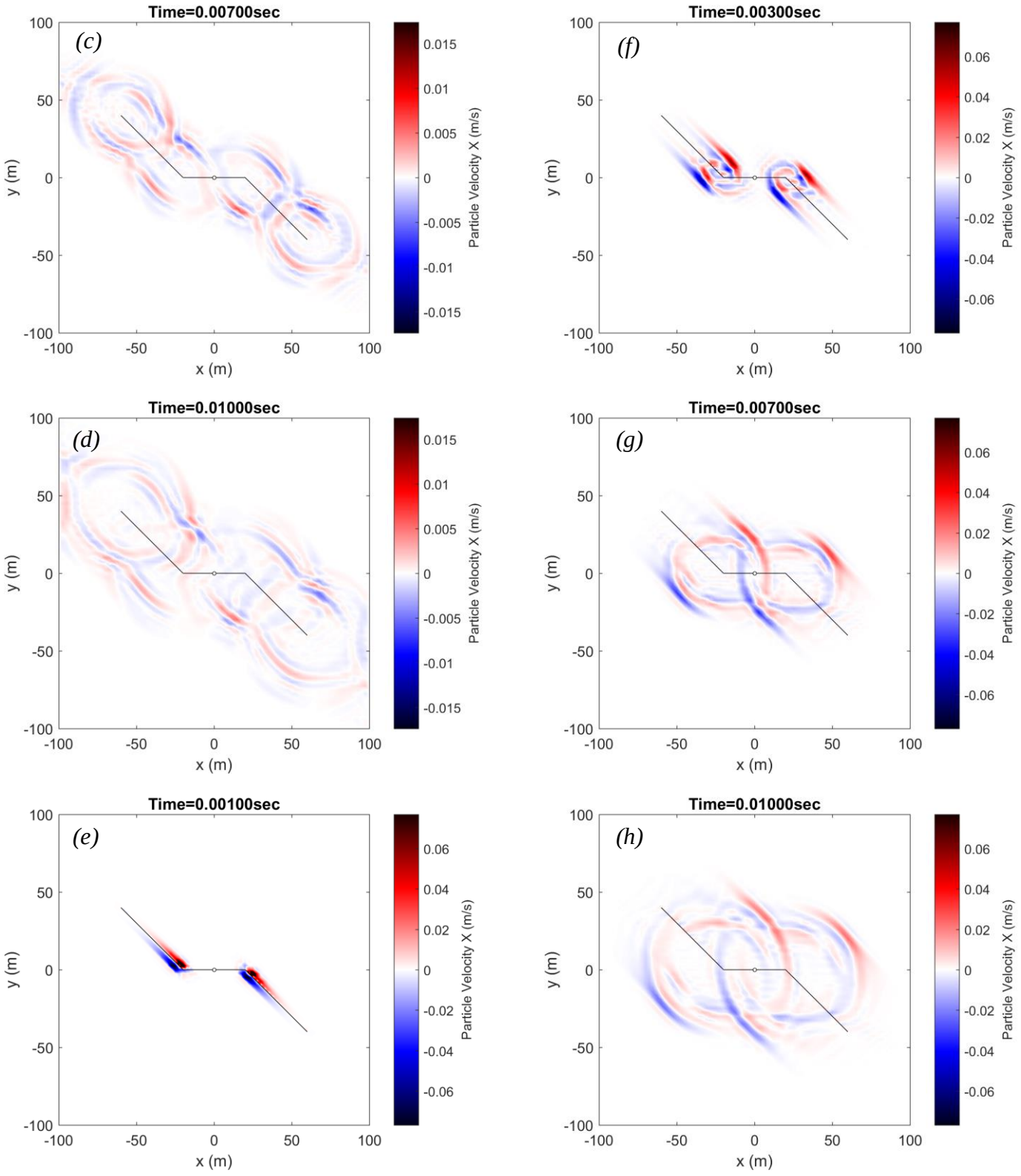

Fig.5. Snapshots of particle velocity along X taken at four different time steps since the onset of shear rupture. Time is shown at the top of each figure. (a)~(d) Case 1; (e)~(h) Case 2. The source of rupture largely coincides with where the maximum fluid pressure occurs.

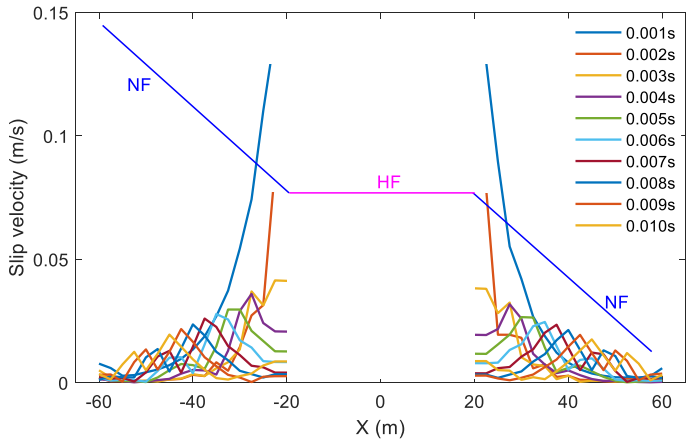

Fig.6. Slip velocity along the two natural fractures at 10 selected time steps since the onset of rupture in Case 2. The horizontal axis is the distance along X (same as the model domain).

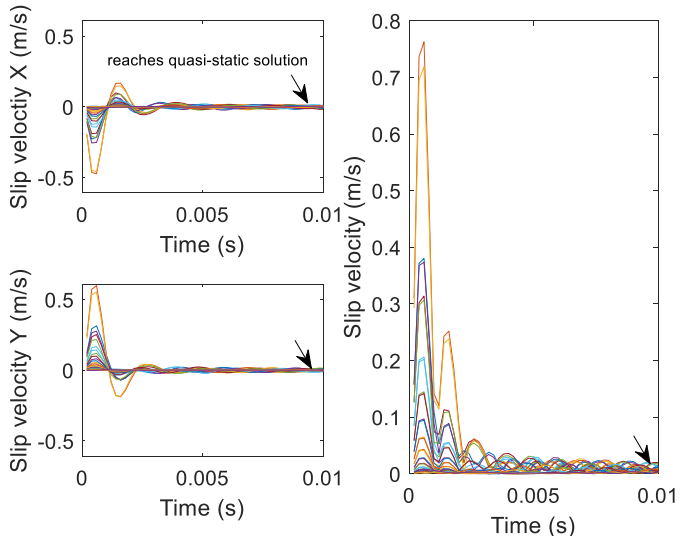

Fig.7. Temporal evolution of slip velocity in Case 2. Slip velocity at all pairs of nodal points on the natural fractures is plotted. X and Y components indicate the motion of the lower fracture face relative to the upper fracture face.

It can also be seen from Fig.7 that at the end of the dynamic modeling (0.01 second), the slip velocity decays to near 0, indicating dynamic changes dissipate on the natural fractures around 0.01 second. For comparison, we also solve for the quasi-static solution of the same rupture problem by dropping all the time-dependent terms and simply solving the remaining of the equation. For comparison, we show in Fig.8 the slip profile obtained at the end of the dynamic modeling and the profile obtained from the quasi-static solution. We observe no noticeable differences. Since slip profile can be particularly useful for calculating certain (micro)seismic source parameters (as will be shown in 3.5), the result here suggests that the use of the quasi-static solution of a rupture problem is sufficient for such purposes.

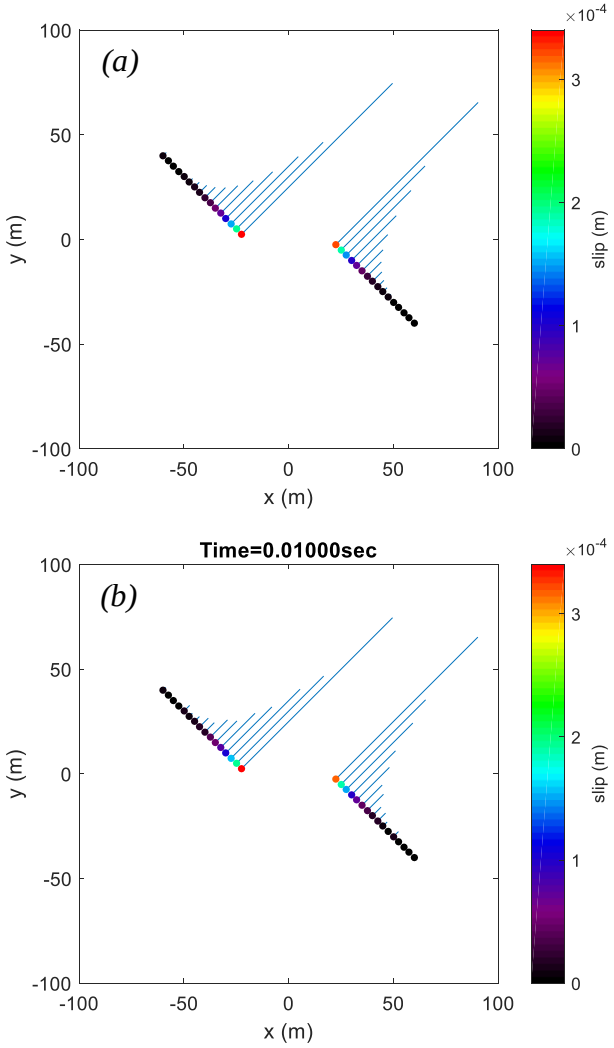

Fig.8. Slip profile along the two natural fractures in Case 2. Color indicates the magnitude of slip. (a) Quasi-static solution; (b) Dynamic solution at 0.01 second since the onset of rupture. This suggests that 0.01 sec after rupture inception is sufficiently long for the dynamics changes to dissipated on rupture sources and for the dynamic solution to converge to the quasi-static solution.

4. MICROSEISMIC SOURCE RESPONSES AND SENSITIVITY TO FRACTURE HYDRAULIC PROPERTY

4.1. Source Mechanism Suggested by Waveforms

Using again Case 2 as an example, we plot the waveforms (particle velocity with time) recorded at locations of the two sets of seismometers shown in Fig.1 (see Fig.9). Note that the distribution of the seismometers permits sampling of the full focal sphere, minimizing the likelihood of sampling bias in the following analysis. Note also that the mechanical parameters and the density of the fluid-solid mixture provided in Table 1 yield a P wave velocity of 4382 m/s and a S wave velocity of 2530 m/s, respectively. The details of calculating the two velocities are omitted here.

The minimum distances from the rupture source (shown to be at the intersections of the hydraulic fracture and the natural fractures, see Fig.5 (e)) to the first and the second set of seismometers are 10 m and 40 m, respectively. One would then anticipate the earliest arrival of the P phase and the S phase to be around 0.0023 sec and 0.0040 sec within the first set, and around 0.0091 sec and 0.0158 sec within the second set. As can be seen, the modeled P phase (first arrival) and S phase (second arrival) agree well with what is anticipated. Interestingly, one curious observation is that the P phase is dominant in nearly all directions, while the S phase is substantially weaker. In other words, the P/S ratio is predominantly above 1 regardless of the position on the focal sphere. This suggests a marked non-double-coupled component in the source rupture mechanism, which, in return, underscores the importance of using flow-driven stress for the fluid-induced rupture modeling. In this case, because the equivalent body force, the pressure gradient, is largely perpendicular to the natural fractures, the focal mechanism is radically different from that of a natural seismic event where the driving force is predominantly the shear traction along a fault. Our modeling thus provides some explanations for some recent studies where the inverted focal mechanisms of induced seismic events show a significant volumetric component (e.g., Zhao et al., 2014; Martínez-Garzón et al., 2017).

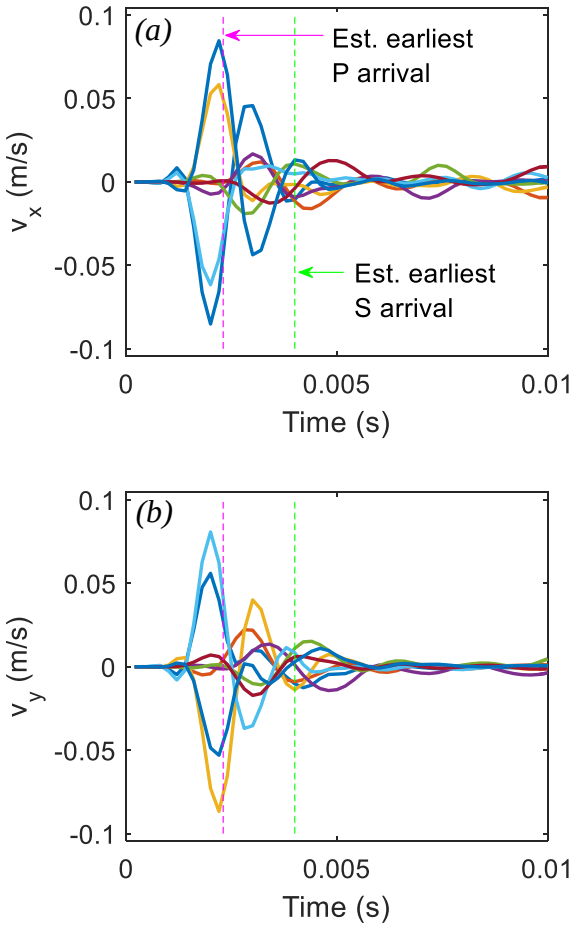

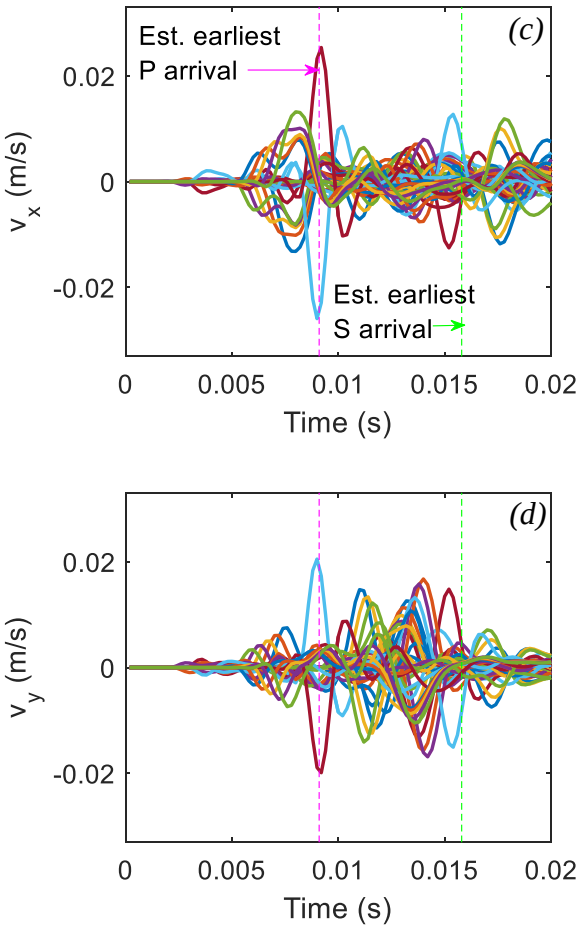

Fig.9. Modeled waveforms (X and Y component) at designated locations in Case 2. (a)&(b) Seismometer set 1; (c)&(d) Seismometer set 2. The anticipated earliest P and S phase arrival times within each set are also marked.

4.2. Representative Source Parameters

Using the standard seismic source parameter relationships and scaling laws, here we calculate a few representative source parameters, specifically, seismic moment M_0, moment magnitude M_w, and static shear stress drop $\Delta\tau$, which are given by the following:

$$M_0 = \sum_j G_f D_j^{QS} L_j W \tag{10}$$

$$M_w = \frac{2}{3}\left(\lg M_0 - 9.1\right) \tag{11}$$

$$\Delta\tau = M_0 \left[\frac{\pi(\lambda+2\mu)}{4(\lambda+\mu)} W^2 L\right]^{-1} \tag{12}$$

where G_f is the shear modulus of the fracture, L_j is the length of the jth segment on the fracture, D_j is the corresponding amount of slip, subscript QS indicates quasi-static solutions, L and W are the fracture length and width, λ and μ are the Lame's constant and shear modulus of the surrounding medium (same as that in Table 1).

For illustration, the parameters are chosen as: G_f=1GPa, W=1m (unit length out of plane), and the others are the same as before. Note in Eq.(10), we use the quasi-static solution, which is the asymptote of the dynamic solution and is sufficient for calculating these parameters (see Fig.8). Note also that Eq.(12) is derived for a rectangular dip-slip fault. The result is shown in Fig.10.

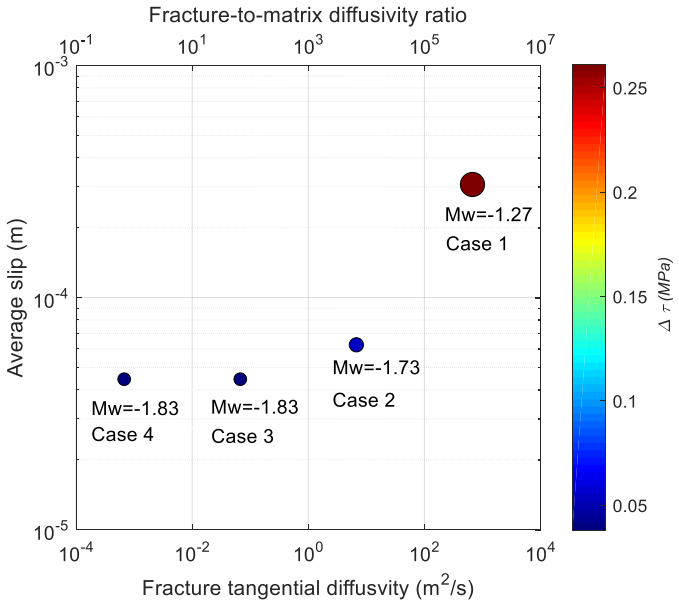

Fig.10. Sensitivity of representative source parameters to the tangential diffusivity of the natural fractures. The top horizontal axis shows the fracture tangential diffusivity nondimensionalized by the average matrix diffusivity.

The moment magnitude ranges from -1.27 to -1.83, and the stress drop from 0.05MPa to 0.25MPa. In the log-log space, the decrease in the fracture tangential diffusivity leads to a negative-exponential drop in the average slip. This trend levels off when the fracture tangential diffusivity drops to the order of 0.01 m^2/s, which is only one order of magnitude above the (average) matrix diffusivity.

4.3. Time of Activation

The time of activation is defined here as the time of onset of dynamic shear rupture. Following the procedures demonstrated in 3.3, we determine the time of activation for all four cases. The result is shown in Fig.11. In the log-log space, the time of activation increases almost linearly as the fracture tangential diffusivity drops until it reaches to the level that is one order of magnitude higher than the matrix diffusivity. However, it is worth noting that such an observation is heavily case-dependent, as the time of activation also depends on a variety of other factors, including the initial stress state, the location of a fracture relative to the injector, the orientation of fracture relative to the stress state, the fracture frictional properties as well as the hydraulic and mechanical properties of the surrounding porous matrix.

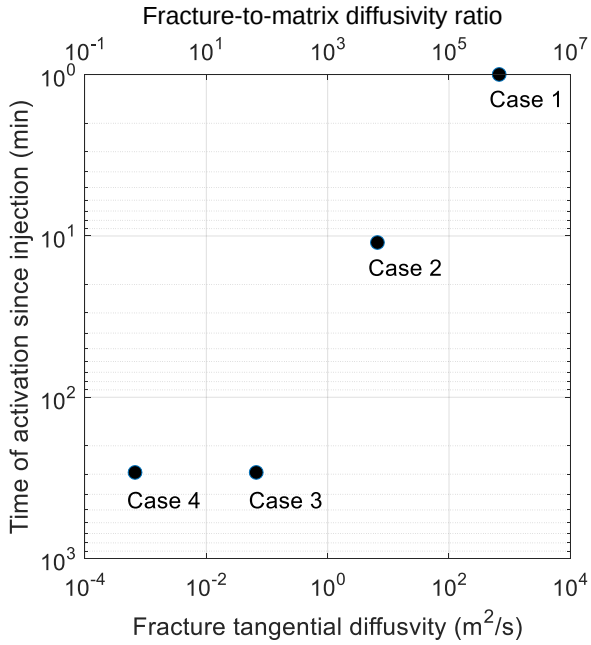

Fig.11. Sensitivity of the time of activation to the tangential diffusivity of the natural fractures. The top horizontal axis shows the fracture tangential diffusivity nondimensionalized by the average matrix diffusivity.

4.4. Estimating Permeability Changes

The change in fracture tangential permeability can be estimated using the cubic law:

$$\delta k_{f\tau} = \frac{1}{12}\left[(b+\delta b)^2 - b^2\right] \tag{13}$$

where δb is the increment in fracture aperture.

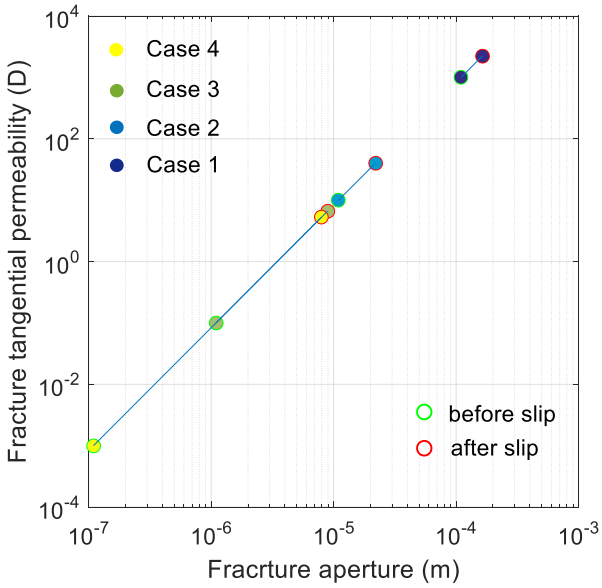

Fig.12. Estimated permeability changes in all cases

Because we impose contact conditions on the natural fractures and model only the shear (mode II) dislocation, we are unable to obtain δb directly. Here, we assume a commonplace dilatational angle β=10°, and estimate δb

as δb=average slip× $tan(\beta)$. The estimated changes in fracture tangential permeability for all cases are given in Fig.12. We observe an increase by four-, two-, one- and half order(s) of magnitude from Case 1~Case 4, suggesting permeability enhancement can be substantial on fractures with low initial permeability, but less so on fractures with high initial permeability.

5. SUMMARY AND CONCLUSION

In this study, we utilized a comprehensive numerical modeling framework to model fluid-induced (micro)seismicity on pre-existing discontinuities embedded in a fully saturated poroelastic medium. Our modeling covers the full spectrum of the physical process, including fluid flow, flow-driven quasi-static triggering and flow-driven co-seismic dynamic shear rupture. True discontinuities are explicitly represented throughout the modeling. We demonstrated how to connect these sub-processes in a fluid-to-solid coupled manner, and highlighted the importance of using a flow-driven full stress tensor arising from the pressure gradient as the input in the analysis of quasi-static triggering and dynamic rupture. For example, our modeling suggests that the curious non-double-couple component in typical focal solutions of fluid-induced seismic events can be directly attributed to the flow-driven stress. If the fluid pressure is supplied directly into the fracture to induce rupture, the P phase is likely to dominate the S phase in all directions.

We constructed four hypothetical cases in which the matrix diffusivity and the fracture diffusivity are on the order of 10^{-3} m^2/s and 10^{-4} ~10^{2} m^2/s, respectively. Given the initial stress state and its relation to the fracture orientation provided in this study, we show that the onset of shear rupture ranges from within 1 minute to near 4 hours since the beginning of injection. Rupture can initiate either along the full length of the discontinuity or from a segment. In the latter case, rupture source coincides with the area subjected to the maximum fluid pressure. The modeled arrival times of both P and S phases agree well with the theoretical calculation. The particle velocity within the domain is on the order of 0.001~0.1m/s. On the discontinuities, the dynamically evolving slip (dislocation) is on the order of 10^{-4} ~10^{-5}m, and converges to the quasi-static solution (of the rupture problem as opposed to the triggering problem) 0.01 second after the onset of rupture. The dynamic slip velocity is on the order of 0.01~0.1m/s. In addition, it is shown that only when the fracture tangential diffusivity is at least one order of magnitude above the matrix diffusivity does it scale with the amount of slip and other microseismic source parameters, including seismic moment, moment magnitude and static shear stress drop. Permeability enhancement is only substantial when the fracture has a low initial permeability to begin with. Lastly, we note that the quantitative aspects of these results are case-dependent as other parameters, including injection pressure and mechanical properties, are also important.

ACKNOWLEDGEMENT

We are grateful to the Stanford Rock Physics and Borehole Geophysics Project for financial support. We also thank the anonymous reviewer for providing many useful comments and suggestions.

REFERENCES

1. Ellsworth, W. L. (2013). Injection-induced earthquakes. *Science*, *341*(6142), 1225942.
2. Stark, M. A., & Davis, S. D. (1996). Remotely triggered microearthquakes at The Geysers geothermal field, California. *Geophysical research letters*, *23*(9), 945-948.
3. Megies, T., & Wassermann, J. (2014). Microseismicity observed at a non-pressure-stimulated geothermal power plant. *Geothermics*, *52*, 36-49.
4. Zoback, M. D., & Zinke, J. C. (2002). Production-induced normal faulting in the Valhall and Ekofisk oil fields. In *The Mechanism of Induced Seismicity* (pp. 403-420). Birkhäuser Basel.
5. Hillis, R. (2000). Pore pressure/stress coupling and its implications for seismicity. *Exploration Geophysics*, *31*(1/2), 448-454.
6. Wang, H. F. (2000). Theory of linear poroelasticity.
7. Cleary, M. P. (1977). Fundamental solutions for a fluid-saturated porous solid. *International Journal of Solids and Structures*, *13*(9), 785-806.
8. Rudnicki, J. W. (1986). Fluid mass sources and point forces in linear elastic diffusive solids. *Mechanics of Materials*, *5*(4), 383-393.
9. Altmann, J. B., Müller, B. I. R., Müller, T. M., Heidbach, O., Tingay, M. R. P., & Weißhardt, A. (2014). Pore pressure stress coupling in 3D and consequences for reservoir stress states and fault reactivation. *Geothermics*, *52*, 195-205.
10. Marck, J., Savitski, A. A., & Detournay, E. (2015). Line source in a poroelastic layer bounded by an elastic space. *International Journal for Numerical and Analytical Methods in Geomechanics*, *39*(14), 1484-1505.
11. Segall, P. (1985). Stress and subsidence resulting from subsurface fluid withdrawal in the epicentral region of the 1983 Coalinga earthquake. *Journal of Geophysical Research: Solid Earth*, *90*(B8), 6801-6816.

12. Segall, P., & Fitzgerald, S. D. (1998). A note on induced stress changes in hydrocarbon and geothermal reservoirs. *Tectonophysics*, *289*(1), 117-128.

13. Murphy, S., O'Brien, G. S., McCloskey, J., Bean, C. J., & Nalbant, S. (2013). Modelling fluid induced seismicity on a nearby active fault. *Geophysical Journal International*, *194*(3), 1613-1624.

14. Chang, K. W., & Segall, P. (2016). Injection-induced seismicity on basement faults including poroelastic stressing. *Journal of Geophysical Research: Solid Earth*, *121*(4), 2708-2726.

15. Fan, Z., Eichhubl, P., & Gale, J. F. (2016). Geomechanical analysis of fluid injection and seismic fault slip for the Mw4. 8 Timpson, Texas, earthquake sequence. *Journal of Geophysical Research: Solid Earth*, *121*(4), 2798-2812.

16. Deng, K., Liu, Y., & Harrington, R. M. (2016). Poroelastic stress triggering of the December 2013 Crooked Lake, Alberta, induced seismicity sequence. *Geophysical Research Letters*, *43*(16), 8482-8491.

17. Baisch, S., Vörös, R., Rothert, E., Stang, H., Jung, R., & Schellschmidt, R. (2010). A numerical model for fluid injection induced seismicity at Soultz-sous-Forêts. *International Journal of Rock Mechanics and Mining Sciences*, *47*(3), 405-413.

18. Wassing, B. B. T., Van Wees, J. D., & Fokker, P. A. (2014). Coupled continuum modeling of fracture reactivation and induced seismicity during enhanced geothermal operations. *Geothermics*, *52*, 153-164.

19. Goertz-Allmann, B. P., & Wiemer, S. (2012). Geomechanical modeling of induced seismicity source parameters and implications for seismic hazard assessment. *Geophysics*, *78*(1), KS25-KS39.

20. Heinze, T., Galvan, B., & Miller, S. A. (2015). Modeling porous rock fracturing induced by fluid injection. *International Journal of Rock Mechanics and Mining Sciences*, *77*, 133-141.

21. Catalli, F., Rinaldi, A. P., Gischig, V., Nespoli, M., & Wiemer, S. (2016). The importance of earthquake interactions for injection-induced seismicity: Retrospective modeling of the Basel Enhanced Geothermal System. *Geophysical Research Letters*, *43*(10), 4992-4999.

22. Rinaldi, A. P., & Nespoli, M. (2016). TOUGH2-seed: A coupled fluid flow and mechanical-stochastic approach to model injection-induced seismicity. *Computers & Geosciences*.

23. Riffault, J., Dempsey, D., Archer, R., Kelkar, S., & Karra, S. Understanding Poroelastic Stressing and Induced Seismicity with a Stochastic/Deterministic Model: an Application to an EGS Stimulation at Paralana, South Australia, 2011.

24. White, J. A., & Borja, R. I. (2008). Stabilized low-order finite elements for coupled solid-deformation/fluid-diffusion and their application to fault zone transients. *Computer Methods in Applied Mechanics and Engineering*, *197*(49), 4353-4366.

25. Béchet, É., Moës, N., & Wohlmuth, B. (2009). A stable Lagrange multiplier space for stiff interface conditions within the extended finite element method. *International Journal for Numerical Methods in Engineering*, *78*(8), 931-954.

26. Martin, V., Jaffré, J., & Roberts, J. E. (2005). Modeling fractures and barriers as interfaces for flow in porous media. *SIAM Journal on Scientific Computing*, *26*(5), 1667-1691.

27. Barenblatt, G. I., Zheltov, I. P., & Kochina, I. N. (1960). Basic concepts in the theory of seepage of homogeneous liquids in fissured rocks [strata]. *Journal of applied mathematics and mechanics*, *24*(5), 1286-1303.

28. Warren, J. E., & Root, P. J. (1963). The behavior of naturally fractured reservoirs. *Society of Petroleum Engineers Journal*, *3*(03), 245-255.

29. Jin, L., & Zoback, M. D. (2016, June). Including a stochastic discrete fracture network into one-way coupled poromechanical modeling of injection-induced shear re-activation. In *50th US Rock Mechanics/Geomechanics Symposium*. American Rock Mechanics Association.

30. Jin, L., & Zoback, M. D. (2017). A Hybrid-dimensional computational model of weakly discontinuous fluid flow and flow-driven stress in fractured porous media. Submitted to *Journal of Geophysical Research: Solid Earth*, in review.

31. Givoli, D. (1991). Non-reflecting boundary conditions. *Journal of computational physics*, *94*(1), 1-29.

32. Lysmer, J., & Kuhlemeyer, R. L. (1969). Finite dynamic model for infinite media. *Journal of the Engineering Mechanics Division*, *95*(4), 859-878.

33. Hughes, T. J. (2012). The finite element method: linear static and dynamic finite element analysis. Courier Corporation.

34. Borja, R. I. (2013). *Plasticity*. Springer.

35. Liu, M., & Gorman, D. G. (1995). Formulation of Rayleigh damping and its extensions. *Computers & structures*, *57*(2), 277-285.

36. Zhao, P., Kühn, D., Oye, V., & Cesca, S. (2014). Evidence for tensile faulting deduced from full waveform moment tensor inversion during the stimulation of the Basel enhanced geothermal system. *Geothermics*, *52*, 74-83.

37. Martínez-Garzón, P., Kwiatek, G., Bohnhoff, M., & Dresen, G. (2017). Volumetric components in the earthquake source related to fluid-injection and stress state. *Geophysical Research Letters*, in press.